

# The Las Campanas Infra-red Survey. V. Keck Spectroscopy of a large sample of Extremely Red Objects

M. Doherty,<sup>1\*</sup> A.J. Bunker,<sup>2</sup> R.S. Ellis<sup>3</sup> and P.J. McCarthy,<sup>4</sup>

<sup>1</sup>*Institute of Astronomy, University of Cambridge, Madingley Road, Cambridge, CB3 0HA, U.K.*

<sup>2</sup>*School of Physics, University of Exeter, Stocker Road, Exeter, EX4 4QL, U.K.*

<sup>3</sup>*California Institute of Technology, Astronomy, Mail Stop 105-24, Pasadena, CA 91125, U.S.A.*

<sup>4</sup>*Observatories of the Carnegie Institute of Washington, Santa Barbara Street, Pasadena, CA 91101, U.S.A.*

Released 2005 Xxxxx XX

## ABSTRACT

We present deep Keck spectroscopy, using the DEIMOS and LRIS spectrographs, of a large and representative sample of 67 “Extremely Red Objects” (EROs) to  $H = 20.5$  in three fields (SSA22, Chandra Deep Field South and the NTT Deep Field) drawn from the Las Campanas Infrared Survey. Using the colour cut  $(I - H) > 3.0$  (Vega magnitudes) adopted in earlier papers in this series, we verify the efficiency of this selection for locating and studying distant old sources. Spectroscopic redshifts are determined for 44 sources, of which only two are contaminating low mass stars. When allowance is made for incompleteness, the spectroscopic redshift distribution closely matches that predicted earlier on the basis of photometric data. Our spectra are of sufficient quality that we can address the important question of the nature and homogeneity of the  $z > 0.8$  ERO population. A dominant old stellar population is inferred for 75% of our spectroscopic sample; a higher fraction than that seen in smaller, less-complete samples with broader photometric selection criteria (e.g.  $R - K$ ). However, only 28% have spectra with no evidence of recent star formation activity, such as would be expected for a strictly passively-evolving population. More than  $\sim 30\%$  of our absorption line spectra are of the ‘E+A’ type with prominent Balmer absorption consistent, on average, with mass growth of 5-15% in the past Gyr. We use our spectroscopic redshifts to improve earlier estimates of the spatial clustering of this population as well as to understand the significant field-to-field variation. Our spectroscopy enables us to pinpoint a filamentary structure at  $z = 1.22$  in the Chandra Deep Field South. Overall, our study suggests that the bulk of the ERO population is an established population of clustered massive galaxies undergoing intermittent activity consistent with continued growth over the redshift interval  $0.8 < z < 1.6$ .

**Key words:** galaxies: evolution – galaxies: stellar content – cosmology: large-scale structure of universe – galaxies: distances and redshifts

## 1 INTRODUCTION

One of the major challenges facing the hierarchical models of galaxy formation (e.g. Somerville et al. 2004) is posed by the large number of massive galaxies with apparently well-established stellar populations observed at high redshift (Glazebrook et al. 2004, Cimatti et al. 2004). Galaxies with evolved stellar populations at moderate redshifts ( $z \sim 1 - 2$ ) can be characterized by very red optical-near-infrared colours. The first examples were identified shortly

after the introduction of near-infrared imaging arrays (Elston, Rieke & Rieke, 1988; McCarthy, Persson, & West 1992; Cowie et al. 1990). Spectroscopy of two of the Elston et al. (1988) red candidates revealed them to be luminous evolved galaxies at  $z \sim 0.8$  (Elston et al. 1989). More distant red galaxies with evolved populations were later identified from deep radio surveys (Dunlop et al. 1996).

The optical-to-near-infrared colour selection appears to yield a mixture of evolved systems and actively star-forming galaxies with substantial internal reddening (see McCarthy 2004 for a review). The prototype of the latter class (ERO J164502+4626.4) was identified by its extremely red  $R - K$

\* email:md@ast.cam.ac.uk

colour by Hu & Ridgway (1994). Subsequent spectroscopy and sub-mm observations revealed this system to be a star-forming galaxy at  $z = 1.44$  (Graham & Dey 1996; Cimatti et al. 1998, Dey et al. 1999).

Earlier papers in this series (McCarthy et al 2001, Firth et al. 2002; Chen et al. 2002) presented source counts, angular clustering and photometric redshifts for objects selected via optical-near infrared colours using the Las Campanas Infra-red Survey (LCIRS) – one of the first to use a panoramic near-infrared camera. This work has been complemented by independent surveys of  $K$ -band selected samples (e.g. Cimatti et al. 2002 – K20; Yan et al. 2003 ; Abraham et al. 2004 – GDDS). Although the abundance of EROs is less than that implied if all of the present-day spheroidal galaxies followed a passive evolutionary track from high redshift, it is much higher than that predicted by current semi-analytical models (Firth et al. 2002; see also Cimatti et al. 2002).

Strong clustering has been observed for the ERO population, with amplitudes up to 10 times that seen in the equivalent flux-limited sample (see e.g. Daddi et al. 2000, Firth et al. 2002). On the basis of photometric redshifts, Firth et al. (2002) and McCarthy et al. (2001) derived comoving correlation lengths of  $r_o \approx 6 - 10h^{-1}$  Mpc (where  $h=H_0/100$  km s $^{-1}$  Mpc $^{-1}$ ), comparable to that for early-type galaxies at low redshift. Daddi et al. (2002) infer a similar, although somewhat larger, clustering scale on the basis of Passive Luminosity Evolution (PLE) models of the redshift distribution of the K20 sample.

Spectroscopic data has played a key role in furthering our understanding of the ERO population. Dunlop et al. (1996) and Spinrad et al. (1997) used low resolution spectroscopy to infer an age in excess of 3.5 Gyr for the radio-selected red galaxy LBDS 53W091 at  $z \sim 1.5$ . More recent intermediate dispersion spectra for co-added samples of fainter colour-selected objects at  $1.3 < z < 2$  also point towards early formation redshifts for a significant fraction of the red population (McCarthy et al. 2004; Cimatti et al. 2004).

The goal of this paper is to build on the earlier LCIRS photometric studies of EROs, using deep Keck spectroscopy. We investigate the redshift distribution and spectroscopic properties of a representative subset of the ERO population. In order to verify and further exploit the earlier work, our spectroscopic targets were selected from three of the LCIRS fields according to the same  $I - H$  colour cut (McCarthy et al. 2001).

With the resulting spectroscopic sample we aim to:

- i) verify that the  $I - H$  colour selection is optimal for selecting passively evolving galaxies at  $z > 1$ ,
- ii) determine the redshift distribution of the population and compare it with that determined photometrically,
- iii) examine the spectroscopic nature of EROs with respect to the (perhaps idealized) view that such a colour criterion locates a passively-evolving population of sources destined to emerge as present-day spheroidal galaxies.

It should be borne in mind that spectroscopic (or morphological) studies can present an incomplete picture of the evolutionary history of a given population. The age of a stellar population need not necessarily coincide with the age of the assembled mass. In particular, a spectral classifica-

tion indicative of an established or aged stellar population need not necessarily correspond to a morphological elliptical. However, spectral diagnostics of recent activity can be invaluable indicators of continuing growth. Our purpose in this paper is largely to explore the spectroscopic *homogeneity* of the ERO population as well as the extent to which the idealized picture of a passively-evolving component can be made to fit the data. We will examine and compare the morphological information on a similar population in the next paper in this series (Doherty et al. *in prep.*)

A plan of the paper follows: in Section 2 we present the sample selection and in Section 3 we detail the Keck spectroscopic observations and their reduction. Section 4 presents the inferred redshift distribution taking into account incompleteness effects. We analyze our results in terms of our primary objectives (above) in Section 5. Our conclusions are presented in Section 6.

Unless otherwise stated, throughout the paper we use the standard “concordance” cosmology of  $\Omega_M = 0.3$ ,  $\Omega_\Lambda = 0.7$ , and  $H_0 = 70$  km s $^{-1}$  Mpc $^{-1}$ . All magnitudes are on the Vega system.

## 2 SAMPLE SELECTION

Our selection of Extremely Red Objects is drawn from three (out of a possible five) LCIRS fields at high Galactic latitude accessible at the Keck observatory: the Chandra Deep Field South (CDF-S; Giacconi et al. 2001 ), the NTT Deep Field (Arnouts et al. 1999 ) and SSA22 (part of the CFRS redshift survey, Lilly et al. 1995 ).

As discussed, we employ the same colour criterion ( $I - H > 3$ ) for EROs as that adopted in the earlier photometric study by McCarthy et al. (2001). Figure 1 demonstrates that this colour cut is designed to select passive objects with redshifts  $z > 1$  and starbursts with substantial dust reddening. To facilitate a reasonable success rate with optical spectroscopy, we adopted a magnitude limit of  $H = 20.5$ . At this limit, the LCIRS survey is close to 100% complete (see discussion in Chen et al. 2002 – §4.3 and Figure 5) and galaxies with  $I - H > 3$  comprise roughly  $\sim 10\%$  of the total population, with a surface density of  $\approx 0.8$  arcmin $^{-2}$ .

We briefly recap the photometric data which forms the basis of our sample. The infrared imaging was obtained with the CIRSI camera (Beckett et al. 1998) on the Du Pont 2.5 m telescope at Las Campanas Observatory between 1998 and 2000. CIRSI has 4 HgCdTe 1024 $^2$  infrared (IR) arrays, spaced by 0.9 array widths, with a pixel scale of 0.2 $''$ . By observing a  $2 \times 2$  mosaic, a contiguous 13 $\times$ 13 arcmin (170 arcmin $^2$ ) field was surveyed. In the case of SSA22, only imaging data from half the area was reduced in time to select EROs for LRIS mask manufacture for our October 2001 observing run. Hence the total survey area from which we built catalogues of EROs is 425 arcmin $^2$ . The photometric data reduction is detailed in Firth et al. (2002) and Chen et al. (2002). In the reduced  $H$ -band images, the typical  $5\sigma$  detection is  $H = 21.5$  in a 3 $''$ -diameter aperture. The optical imaging came from the CFHT 12k Mosaic ( $V$ -,  $R$ - &  $I$ -band for SSA22), the Wide Field Camera on the 2.5 m Isaac Newton Telescope (for NTT), and the Mosaic-II camera on the CTIO 4 m ( $V$ -,  $R$ -  $I$ - &  $z$ -band for CDF-S). The optical and

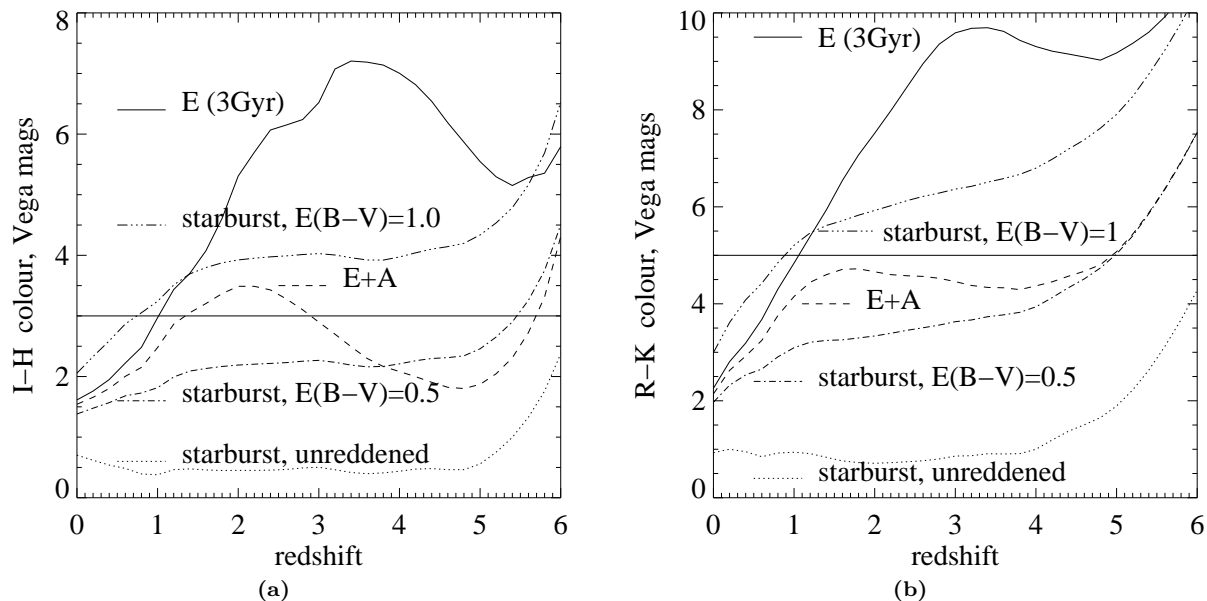


**Figure 1.** (a) Evolution in the predicted ( $I - H$ ) colours (Vega system) for various stellar populations, produced with Bruzual & Charlot's (2000) synthesis code assuming a Scalo (1986) initial mass function. The elliptical (E) spectral energy distribution (solid line) has an age of 3 Gyr. The E+A spectrum is equivalent but viewed 100 Myr after a burst of star formation involving 5% of the stellar mass. The starburst galaxy assumes an exponential star formation history with an e-folding time of 1 Gyr, viewed 10 Myr after the onset of star formation. Reddening of  $E(B - V) = 0.5$  and 1.0 have been applied using Calzetti's (1997) prescription. The  $I - H > 3$  colour criterion (shown) is designed to select passive objects with redshifts  $z > 1$  and highly reddened starbursts with  $z > 0.7$ . For comparison, the equivalent tracks for an  $R - K > 5$  colour cut are shown in the adjacent panel (b). The essential difference evident here is that E+A type galaxies would not be expected to occur in an  $R - K > 5$  selected sample.

infrared images were registered and distortion-corrected to an astrometric frame determined using the Digitized Sky Survey. Colour selection was performed using version 2.2.1 of the SExtractor package (Bertin & Arnouts 1996) in two-image mode with a fixed aperture of  $3''$  diameter.

Spectroscopy was performed at Keck with both the Low Resolution Imaging Spectrograph (LRIS; Oke et al. 1995) and the Deep Imaging Multi-Object Spectrograph (DEIMOS, Faber et al. 2003; Phillips et al. 2002). The  $5' \times 7'$  LRIS slitmask field is much smaller than a CIRSI tile, whereas the DEIMOS field covers  $16.5' \times 5'$  (i.e., about half the area surveyed in a CIRSI tile). In selecting sources for multi-object spectroscopy, the astrometric centre and position angle of the masks were optimised within the LCIRS fields to maximize the number of candidate EROs. We discuss later the possible biases that this may bring to our analyses. The minimum slit length was set to  $6''$ , and the selection was determined entirely by geometric constraints. In the event of a slit clash higher priority was given to the brighter source (in  $I$ ).

The fraction of EROs within the field of view of each spectrograph that could be incorporated onto a mask was roughly 50% (29/73 in NTT, 16/31 in CDFS, 30/55 in SSA22). The angular distribution of EROs is shown in Figure 2. Part of the DEIMOS mask for CDFS was taken up with targets for another program involving spectroscopy of  $i'$ -band drop-out redshift  $\sim 6$  galaxies (see Bunker et al. 2003; Stanway et al. 2004), which necessitated part of the mask falling outside of the LCIRS field. The spectroscopically surveyed area from each LCIRS image is thus:

$\approx 80 \text{ arcmin}^2$  for NTT;  $\approx 60 \text{ arcmin}^2$  for CDFS; and  $\approx 60 \text{ arcmin}^2$  for SSA22, a total of about  $200 \text{ arcmin}^2$ .

### 3 SPECTROSCOPY

#### 3.1 LRIS multi-object spectroscopy

We obtained long-slit spectroscopy of 41 EROs on the nights of 2001 October 22–24 UT using LRIS (Oke et al. 1995) at the f/15 Cassegrain focus of the 10-m Keck I telescope. Spectra were obtained for 11 EROs in CDFS (including 6 which overlapped with the later DEIMOS sample, Section 3.2), and for 30 EROs in SSA22 (using 2 different masks). Full details are given in Table 1.

The LRIS red-arm detector is a Tek 2048<sup>2</sup> CCD with  $24 \mu\text{m}$  pixels. The angular scale is  $0''.212 \text{ pixel}^{-1}$ , and the CCD was read out in two-amplifier mode. Observations were obtained using the  $600 \text{ line mm}^{-1}$  grating in first order blazed at  $7500 \text{ \AA}$ , producing a dispersion of  $1.24 \text{ \AA pixel}^{-1}$ . The reference arc lamps and sky-lines have a full width at half maximum (FWHM)  $\approx 5\text{--}8 \text{ \AA}$  (the spectral focus being best at the central wavelength). For objects that fill a  $1''$ -wide slit, the velocity width of a spectrally unresolved line is  $\text{FWHM} \approx 220\text{--}300 \text{ km s}^{-1}$ . A wider  $1.5''$  slit was used for CDFS and SSA22#1, producing slightly lower spectral resolution ( $\sim 400 \text{ km s}^{-1}$  FWHM). The grating was tilted to place a central wavelength of  $\lambda = 8200 \text{ \AA}$  on the detector (for slits in the centre of the mask), sampling the wavelength range  $7000\text{--}9000 \text{ \AA}$  in all targets, with up to  $\approx 500 \text{ \AA}$  either end depending on the position of the slit on the mask.

Field	Field Centre (J2000)	Instr.	date/time	total exptime	PA (deg)	slit width (arcsec)	No. targets
SSA22#1	22:17:41.9 00:13:53	LRIS	22–24 Oct 2001	16ks	10	1.5	16
SSA22#2	22:17:45.0 00:18:45	LRIS	22–24 Oct 2001	26ks	-20	1.0	12
CDFS	03:32:26.1 -27:43:24	LRIS	22–24 Oct 2001	18ks	-25	1.5	11 <sup>1</sup>
CDFS	03:32:35.2 -27:47:52	DEIMOS	8-9 Jan 2003	20 ks	6	1.0	15 <sup>2</sup>
NTT	12:04:10.2 -07:26:06	DEIMOS	8-9 Jan 2003	19.2 ks	-50	1.0	23

**Table 1.** Summary of Spectroscopic Observations

We simultaneously obtained exposures with the blue arm of LRIS (read in one-amplifier mode, with the 300 lines  $\text{mm}^{-1}$  grating blazed at 5000 Å), using a dichroic beam-splitter at 6800 Å. However, due to the red nature of our objects, there was little or no flux at  $\lambda \lesssim 6000$  Å.

The total integration times are given in Table 1. These were broken into individual exposures of duration 2000 s to enable more effective cosmic ray rejection. The telescope was dithered by  $\pm 3''$  along the slit between integrations to facilitate the removal of fringing in the red and the elimination of bad pixels. The observations spanned an airmass range of 1.00 – 1.5. The seeing had a FWHM =  $0''.6$ – $1''.0$  over the course of the night. Spectrophotometric standard stars HZ 4, G191B2B & Feige 110 (Massey et al. 1988; Massey & Gronwall 1990) were observed at similar airmass to determine the sensitivity function for flux calibration.

Each frame was bias subtracted according to values determined from the overscan region and converted to electrons by the gain appropriate to each amplifier. A high signal-to-noise averaged dark current frame was then subtracted. Normalized flat fields were derived from exposures taken with a halogen lamp immediately after the science exposures. For each dither position the average of the other two positions was subtracted, to remove the fringing pattern (which is approximately fixed in space and does not vary significantly with time), while preserving the object signal. Residual sky subtraction was performed by fitting a low-order polynomial to each detector column (parallel to the slit). Individual nod positions were registered and combined using a cosmic ray rejection algorithm, and data on the same mask from different nights were added using inverse-variance weighting.

One-dimensional spectra were extracted using the IRAF *apall* package: extraction widths of 6 pixels ( $1.3''$ ) were used, and the curvature of individual object spectra was “traced” across the array. Wavelength calibration was obtained from Ne+Ar reference arc lamps, and a fourth-order polynomial fit to the centroids of 40 arc lines created a wavelength solution with *rms* residuals of  $0.3$  Å.

### 3.2 DEIMOS multi-object spectroscopy

We also obtained slit-mask spectra of 38 EROs using the DEIMOS spectrograph (Faber et al. 2003; Phillips et al. 2002) at the Nasmyth focus of the 10-m Keck II telescope. We used one slitmask each on the CDFS field and the NTT field, targeting EROs within the  $16.5 \times 5$  arcmin DEIMOS field. Details are given in Table 1. Each slit was  $1''$  wide, with a minimum slit length of  $6''$ . DEIMOS has 8 MIT/LL  $2k \times 4k$  CCDs with  $15 \mu\text{m}$  pixels and an angular scale of  $0.1185'' \text{pix}^{-1}$ .

Observations were obtained using the Gold 1200 line  $\text{mm}^{-1}$  grating in first order tilted to a central wavelength of 8400 Å with a dispersion of  $0.32 \text{ Å pixel}^{-1}$ . Each spectrum spanned  $\approx 2600$  Å and for all targets covered  $\lambda\lambda_{\text{obs}} 7000 - 9000$  Å. A small  $8 \text{ Å}$  region in the centre of the wavelength range falls in the gap between two CCDs. We used the OG550 order-blocking filter to remove all light at wavelengths short-ward of 5500 Å, to avoid contamination by second-order light.

The spectral resolution is  $\Delta\lambda_{\text{FWHM}}^{\text{obs}} \approx 1.4 \text{ Å}$  ( $\Delta v_{\text{FWHM}} \approx 55 \text{ km s}^{-1}$ ), as measured from the sky lines. The seeing was typically  $0''.6 - 0''.9$  FWHM, i.e. smaller than the slit width, implying that the resolution quoted above is a slight overestimate.

The seeing was typically in the range  $0''.6 - 0''.9$  FWHM, smaller than the slit width of  $1''.0$ . As the seeing disk was smaller than the slit width the true resolution is somewhat better for a source which does not fill the slit.

Observations were divided into individual exposures of duration 2400 s. The telescope was dithered  $1.5''$  along the slit between integrations. Flux calibration and telluric correction were carried out using observations of the spectrophotometric standard HZ 44 (Massey et al. 1988; Massey & Gronwall 1990). The flux calibration was checked using the spectra of the five alignment stars of known broad-band photometry ( $I \approx 17 - 19$  mag), which were used to position the masks through  $2'' \times 2''$  alignment boxes. Wavelength calibration was obtained from Ne+Ar+Hg+Kr reference arc lamps.

Most of the spectra were reduced using v1.1.4 of the DEEP2 data pipeline<sup>3</sup>. The pipeline rectifies the slitlets, which are curved on the detector, by tracing the slit edges, then flat field corrects and determines a 2-D wavelength solution for each slit. For each of the science frames, a *b*-spline sky model is fitted and subtracted. The frames are finally combined resulting in a mean, sky-subtracted, cosmic ray rejected 2D spectrum for each slitlet.

We found the pipeline failed for around 25% of our data, largely because our observational strategy deviated from that employed for the more routine DEEP2 survey. Our slits were long and untilted; this caused the *b*-spline solutions to diverge. In those cases where the sky subtraction from the automated pipeline was inadequate, we re-reduced the slitlets using standard IRAF long-slit procedures (as detailed in Section 3.1).

<sup>3</sup> <http://astron.berkeley.edu/~cooper/deep/spec2/>

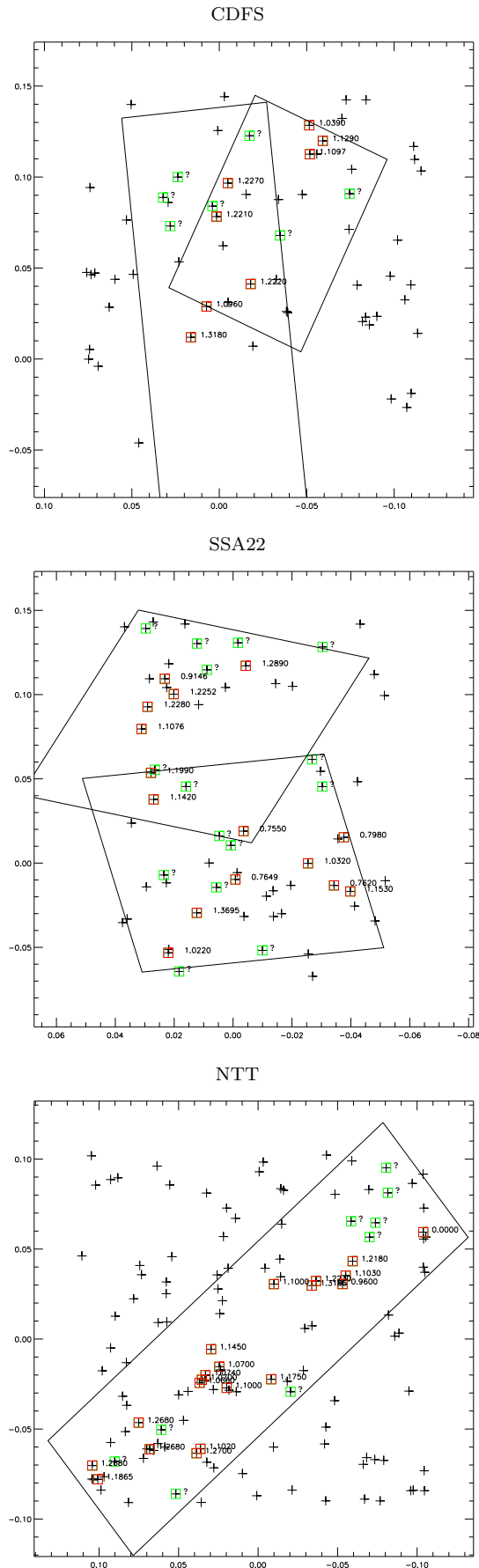


**Figure 2.** Distribution of EROs for the three LCIRS fields. Candidates in the CDFS, SSA22, and NTT fields are marked with crosses. Where redshifts were identified the boxes are marked accordingly (otherwise indicated '?'). The areas delineated refer to the spectroscopic footprints of the slit-mask.

## 4 REDSHIFT DISTRIBUTION AND COMPLETENESS ISSUES

In this section we discuss the determination of spectroscopic redshifts and present the redshift distribution for our  $I - H > 3$ ,  $H < 20.5$  sample taking into account various sources of incompleteness.

A complete inventory of all our spectra is given in Figures 15, 16, and 17.

### 4.1 Redshifts and Spectral Classification

1-D spectra were extracted over a width of  $1.3''$ . Sky residuals due to imperfect sky subtraction were masked out and interpolated over. In both the LRIS and DEIMOS spectra typically around  $\sim 10\%$  of the array was masked out. Although the DEIMOS resolution is much higher, we used a harsher sky threshold in the masking as the background subtraction by the pipeline was not always quite adequate (Section 3.2).

To facilitate redshift measurement, we compared with early and late type spectral templates from the Gemini Deep Deep Survey (GDDS; Abraham et al. 2004) and a luminous red galaxy template from the Sloan Digital Sky Survey (SDSS; Eisenstein et al. 2003), matching spectral features and the general continuum shape by visual inspection. Typically, identifications were based on the  $4000\text{\AA}$  break, CaII H&K ( $3968/3933\text{\AA}$ ) absorption, G-band ( $4300\text{\AA}$ ) absorption, or the  $[\text{O II}]\lambda\lambda 3726.2, 3728.9\text{\AA}$  emission line doublet which was resolved in the DEIMOS data.

The redshifts for each of the 3 fields are summarised in Tables 3, 4 and 5. Quality flags have been assigned as follows: 0=fail, 1=uncertain (based on weak feature(s)), 2=probable (based on one reliable feature), 3=secure (based on more than one certain feature) and -1=possible high redshift ( $z > 1.4$ ) on the basis of a strong continuum detection but no features (discussed below). The redshift distribution for the whole sample is shown in Figure 3. Two (5%) of our sources are Galactic stars.

Of 75 objects observed in the three fields, we were able to identify redshifts for 44 sources (including two stars). Of these, seven identifications ( $\sim 15\%$ ) have the lowest quality flag (1=uncertain). Where we could not identify redshifts, it was usually because the continuum was too faint to detect absorption lines. In five cases we *do* detect significant continuum but fail to identify any spectral features (quality=-1). Most likely these are higher redshift ( $z > 1.4$ ) sources where the most prominent spectral features are redshifted beyond our spectroscopic range. In a few cases ( $\approx 5\%$ ), there were data acquisition or reduction problems – such as a source falling on top of bad pixel rows on the detector. In SSA22 two objects fell right at the edge of the slit mask and were severely vignettted. In the NTT field, six sources fell on an area of the chip which was misaligned due to one of the alignment stars being significantly off centre (the northern most part of the mask, Figure 2) and the slitlets therefore missed the galaxies. For our statistical analyses we will treat these eight (two in SSA22 and six in NTT) sources as unobserved. Hence, our sample of observed objects is actually 67 in total, for which we obtain 44 redshifts, thereby giving  $\sim 66\%$  completeness. This is comparable to or better than the success rates in other spectroscopic surveys of faint galaxies with

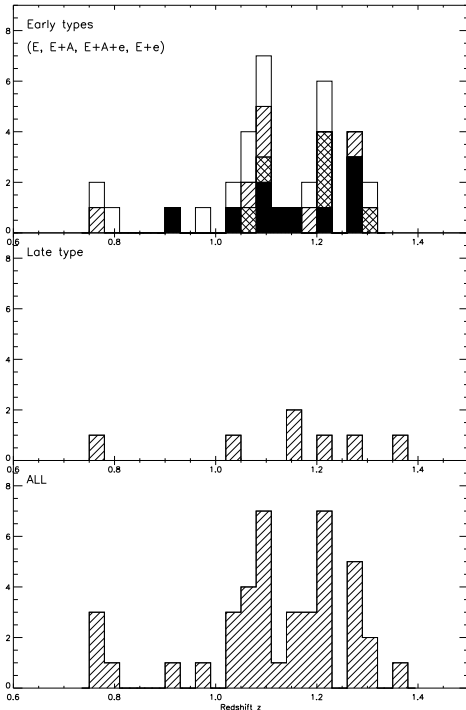


**Figure 3.** Combined redshift distributions across the three LCIR fields for various spectroscopic classes. From bottom to top: all galaxies, late type, early types (subdivided in E, E+A (diagonal fill) / E+A+e (cross-hatched) / E+e(solid fill)).

$R - K > 5$  or  $I - K > 4$  (e.g. equivalent to the K20 survey work which has reached a spectroscopic completeness of 62% to  $K_s < 20$ ,  $R - K_s > 5$  (Cimatti et al. 2002, 2003); see also surveys described in Yan, Thompson, and Soifer 2004; Abraham et al. 2004). We also classified our galaxy spectra according to the prominence of diagnostic spectral features, as follows:

- i) early-type (E): strong absorption features especially Ca II H&K, no detectable [OII] emission and weak or absent Balmer absorption (i.e.  $H\delta$  with rest-frame equivalent width  $< 4\text{\AA}$ ).
- ii) E+A: as early-type (i.) but with enhanced Balmer absorption ( $H\delta$  with rest-frame equivalent width  $> 4\text{\AA}$  (see e.g. Van Dokkum & Ellis 2003 ),
- iii) E+e: as early-type but with weaker Ca II H&K and moderate to strong [O II] emission,
- iv) late-type: showing prominent [OII] emission ( $> 10\sigma$ ,  $f \sim 2.0 \times 10^{-18} \text{erg s}^{-1} \text{cm}^2$ ) and no significant Ca II H&K.
- v) E+A+e ('mixed'): resemble the E+A class of galaxy, but also exhibit [OII] emission, i.e. 'mixed' stellar populations.
- vi) other: stars and AGN. There is only one AGN in our sample, which has been classified by the presence of high ionisation lines ([NeV],[NeIII])

The split in spectral classifications for those sources with redshifts is shown in Table 2.

## 4.2 Effects of Incompleteness

A key question is whether the 34% incompleteness correlates with  $I - H$  colour. For example it might be expected that sources with prominent features and large  $4000\text{\AA}$  breaks would yield redshifts more readily. Figure 4 shows how incompleteness correlates with colour and magnitude and also addresses the question of the extent to which our spectroscopic targets are representative of the overall distribution of EROs. The histograms in  $I - H$  and  $H$ -magnitude show numbers of EROs in the detector footprints in all fields, subdivided into those for which we have identified redshifts, not identified and not observed. It is clear that the subsample of identified redshifts is a representative sample of EROs at least to  $I - H \leq 3.5$  and  $H \leq 20$ , with no bias in colour or magnitude space. There is some apparent incompleteness towards the redder and fainter end of the distribution, which may possibly be populated by  $z > 1.4$  galaxies which are too red and faint to be detected optically.

Of greater concern is the likelihood that some of the 34% of unidentified sources lie at higher redshifts because the principal spectroscopic features are shifted beyond our wavelength range, viz.  $z > 1.4$ . As discussed, a fraction of our sample ( $\sim 10\%$ ) have quality flags of -1 indicating a strong continuum in which features might be expected. A key question is whether most or all of these objects lie beyond  $z \simeq 1.4$ .

We tested for this hypothesis in the CDFS field using the photometric redshift technique described in Daddi et al. (2004). These authors have proposed that galaxies at  $z > 1.4$  will lie in a well-defined region on a  $BzK$  colour-colour diagram. To facilitate the comparison we took F450W ( $B$ ) and F850LP ( $z$ ) photometry from the GOODS-South HST/ACS (Dickinson et al. 2003; Giavalisco et al. 2004) and  $K_s$  band data from the ESO ISAAC survey (Vandame et al., *in prep*). The  $K_s$  band image covers a 13 of our EROs, and of the 6 in this subsample for which we failed to derive redshifts, four lie in the  $BzK$  region for expected  $z > 1.4$  (Figure 5). However, the region is contaminated by three lower  $z$  objects, a somewhat higher fraction than that quoted by Daddi et al. (2004). So while this seems to indicate that some of our unidentified sources most likely do lie at  $z > 1.4$ , the technique is not definitive for a small sample. The result is strengthened however, by the distribution of our galaxies in the  $V - I$  v's  $I - H$  two-colour plane (Figure 6), which is also generally effective in isolating  $z > 1.4$  galaxies (McCarthy 2004).

## 4.3 Comparison with Earlier Work

There have been several redshift surveys of faint objects in our target fields, and consequently there is some small overlap ( $\simeq 20\%$ ) with our ERO sample. As a check on our identifications, we matched our catalogue by coordinates (to within 1 arcsec), with the GDDS sample for the SSA22 field (Abraham et al. 2004) and with the FORS2 spectroscopic sample of Vanzella et al. (2004) and the K20 survey<sup>5</sup> (Cimatti et al. 2002) for the CDFS field. For the FORS2 sample (Table 6), we find good agreement with the five sources in common.

<sup>5</sup> [www.arcetri.astro.it/~k20](http://www.arcetri.astro.it/~k20)

Field	completeness	late type	early type	E+A	E+e	E+A+e	other
CDFS	56%	0	45%	0%	22%	22%	1 star (~ 11%)
NTT	87%	5%	20%	20%	30%	15%	1 star (~ 5%), 1 AGN (~ 5%)
SSA22	54%	40%	27%	13%	13%	7%	0
Whole Sample	66%	16%	27%	13.5%	23%	13.5%	2 stars (5%), 1 AGN (~ 2%)

Table 2. Classification of sources by field.

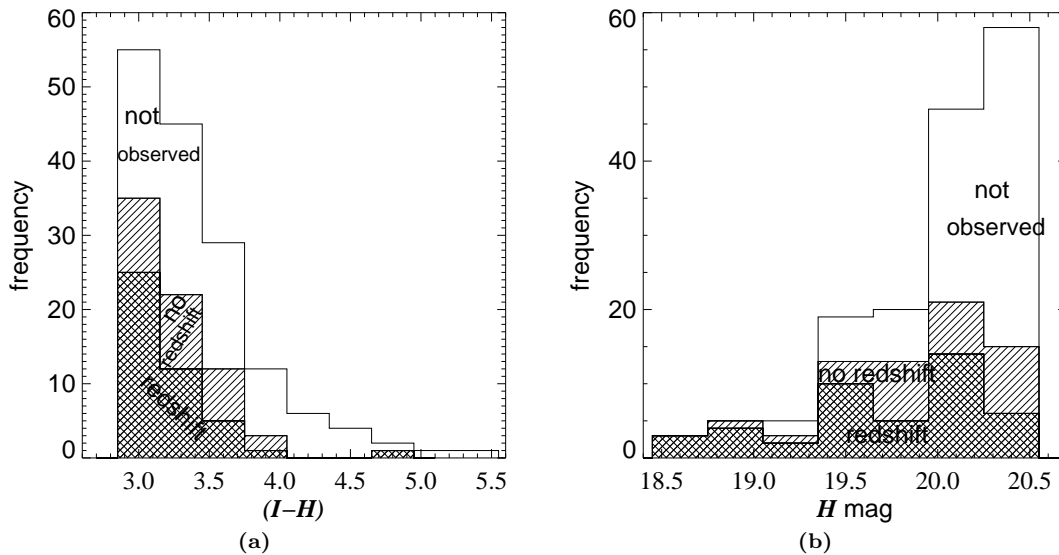


Figure 4. Histograms in (a)  $I - H$  and (b)  $H$  magnitude showing incompleteness trends in our sample. There appears to be some incompleteness towards the red ( $I - H > 3.5$ ) and faintest ( $H > 20$ ) end of the distribution, which may be accounted for by possible  $z > 1.4$  sources which are too red and/or faint to be detected optically.

ID	RA (J2000)	Dec (J2000)	I mag	H mag	Instrument	redshift	quality	nature	comments
939	3 32 14.98	-27 42 25.00	22.45	18.83	Iris	—	0	—	
1276	3 32 19.14	-27 40 40.40	22.00	18.73	Iris	1.1290	3	E+e	
1430	3 32 21.15	-27 41 6.80	22.40	19.35	Iris	1.1097	3	E+A+e	
1447	3 32 21.24	-27 40 9.70	22.55	19.51	Iris	1.0390	1	early	
1665	3 32 24.16	-27 42 11.00	21.90	18.84	Iris	0.0000	3	M star	
2191	3 32 30.51	-27 40 30.40	23.46	20.21	Iris	—	0	—	
2459	3 32 33.87	-27 42 4.10	23.48	20.42	Iris	1.2270	2	early	
2588	3 32 35.62	-27 43 10.20	22.74	19.64	deimos	1.2210	3	E+A+e	
2668	3 32 36.27	-27 42 49.50	23.93	20.18	deimos	—	-1	—	possible $z > 1.4$
2681	3 32 37.18	-27 46 8.20	21.67	18.57	deimos	1.0960	3	early	
2800	3 32 39.61	-27 47 9.00	23.35	20.14	deimos	1.3180	2	early	
3695	3 32 41.64	-27 41 52.10	23.09	19.92	deimos	—	0	—	
3807	3 32 43.92	-27 42 32.40	23.67	19.67	deimos	—	-1	—	possible $z > 1.4$
4071	3 32 42.81	-27 43 28.90	23.80	20.10	deimos	—	-1	—	possible $z > 1.4$
1792	3 32 25.77	-27 43 47.60	23.48	20.28	deimos	—	0	—	
2158	3 32 30.33	-27 45 23.60	22.54	19.44	deimos	1.2220	3	E+e	
I1843 <sup>4</sup>	3 32 26.28	-27 45 36.00	22.78	19.93	deimos	1.2250	3	E+A	
I2897	3 32 38.12	-27 44 32.90	22.48	19.65	deimos	1.2210	2	early	
I2331	3 32 32.97	-27 41 16.90	21.66	18.68	deimos	1.0420	3	E+A+e	
I3063	3 32 39.51	-27 41 17.30	22.71	19.83	deimos	1.0394	3	early	
I2876	3 32 38.43	-27 40 19.40	22.72	19.90	deimos	1.0370	3	early	
I2163	3 32 30.00	-27 47 26.40	23.62	20.19	deimos	0.9900	1	early	

Table 3. CDFS Sample: Quality flags: 0=fail, 1=uncertain, 2=probable, 3=secure, -1= $z > 1.4$ , 6=star. Objects prefixed with an ‘I’ in the above table, were selected with  $R - K > 5$ .

ID	RA (J2000)	Dec (J2000)	I mag	H mag	$I - H$	redshift	quality	nature
275	12 04 22.73	-07 31 15.6	22.90	19.96	2.94	—	-1	poss hi-z
716	12 04 34.60	-07 30 46.3	23.05	19.99	3.06	1.1865	3	E+A
1193	12 04 35.45	-07 30 18.9	22.78	19.69	3.09	1.2680	3	E+e
1218	12 04 32.04	-07 30 10.9	22.56	19.55	3.01	—	-1	poss hi-z
1388	12 04 19.58	-07 29 54.2	23.59	20.07	3.52	1.2700	3	E+e
1494	12 04 26.70	-07 29 46.3	23.13	19.84	3.29	1.2680	3	E+e
1496	12 04 18.98	-07 29 45.4	23.45	20.50	2.95	1.1020	2	early
1962	12 04 24.95	-07 29 07.4	23.41	20.21	3.20	—	-1	poss hi-z
2159	12 04 28.38	-07 28 53.0	23.44	20.07	3.37	1.2680	3	E+A
3249	12 04 14.99	-07 27 43.4	22.41	19.37	3.04	1.1000	3	E+A
3300	12 04 19.11	-07 27 33.4	23.59	20.31	3.28	1.0660	3	early
3456	12 04 18.77	-07 27 27.2	22.71	19.51	3.20	1.0700	3	E+A+e
3464	12 04 08.21	-07 27 26.3	22.27	19.35	2.92	1.1750	3	AGN(?)
3472	12 04 18.22	-07 27 18.1	23.39	19.96	3.43	1.0740	3	E+A
3720	12 04 16.12	-07 27 01.2	23.49	20.15	3.34	1.0700	3	early
4206	12 04 17.36	-07 26 26.2	22.69	19.36	3.33	1.1450	3	E+e
5928	12 04 02.05	-07 24 18.9	23.06	20.15	2.91	1.3185	3	E+A+e
5962	12 04 07.80	-07 24 15.9	23.04	20.12	2.92	1.1000	3	E+e
6052	12 03 57.36	-07 24 15.9	23.06	20.14	2.92	0.9600	1	early
6056	12 04 01.39	-07 24 09.6	23.00	20.01	2.99	1.2230	3	E+A+e
6322	12 03 56.88	-07 23 58.9	22.24	19.20	3.04	1.1030	3	E+e
6696	12 03 55.82	-07 23 30.1	22.64	19.27	3.37	1.2180	1	late
7463	12 03 45.06	-07 22 32.0	23.71	18.99	4.72	0.0000	6	star

Table 4. NTT Sample

ID	RA (J2000)	Dec (J2000)	I mag	H mag	mask#	redshift	quality	nature
403	22 17 49.01	0 22 14.30	23.46	20.44	2	—	0	—
527	22 17 41.50	0 21 43.60	23.58	20.29	2	—	0	—
531	22 17 44.84	0 21 42.00	23.58	20.40	2	—	0	—
713	22 17 40.86	0 20 54.50	23.51	20.42	2	1.2890	2	late
749	22 17 44.03	0 20 45.90	23.52	20.47	2	—	0	—
781	22 17 47.46	0 20 26.90	22.04	18.86	2	0.9146	3	E+e
958	22 17 46.73	0 19 53.90	23.50	20.49	2	1.2252	3	E+A+e
1051	22 17 48.87	0 19 26.90	21.80	18.64	2	1.2280	2	early
1267	22 17 49.36	0 18 39.60	23.26	20.19	2	1.1076	3	E+A
1535	22 17 35.46	0 17 34.60	23.45	19.81	1	—	0	—
1623	22 17 48.27	0 17 12.30	22.92	19.86	1	—	0	—
1655	22 17 48.59	0 17 5.80	23.39	19.85	2	1.1990	1	early
1792	22 17 45.73	0 16 36.60	23.31	19.55	1	—	0	—
1803	22 17 34.62	0 16 36.30	23.37	20.30	1	—	0	—
1920	22 17 48.37	0 16 9.00	23.69	20.10	2	1.1420	1	late
2220	22 17 41.04	0 15 1.30	23.89	20.30	2	0.7550	1	late
2244	22 17 43.02	0 14 51.00	23.46	19.77	1	—	0	—
2260	22 17 32.86	0 14 48.10	22.99	19.50	1	0.7980	2	early
2335	22 17 42.08	0 14 30.80	23.37	19.91	1	—	0	—
2467	22 17 35.79	0 13 52.40	22.12	18.99	1	1.0320	3	E+e
2593	22 17 47.54	0 13 27.50	23.01	19.34	1	—	0	—
2638	22 17 41.71	0 13 18.00	23.32	20.21	1	0.7649	3	E+A
2767	22 17 39.50	0 10 46.50	22.78	19.56	1	—	0	—
2779	22 17 47.18	0 10 41.30	22.89	19.87	1	1.0220	2	late
2993	22 17 44.86	0 12 6.70	22.91	19.88	1	1.3695	2	late
3116	22 17 43.25	0 13 1.10	23.23	19.82	1	—	0	—
3253	22 17 32.34	0 12 52.40	23.25	20.15	1	1.1530	2	late
3378	22 17 33.67	0 13 5.30	23.38	19.54	1	0.7620	1	early?

Table 5. SSA22 Sample

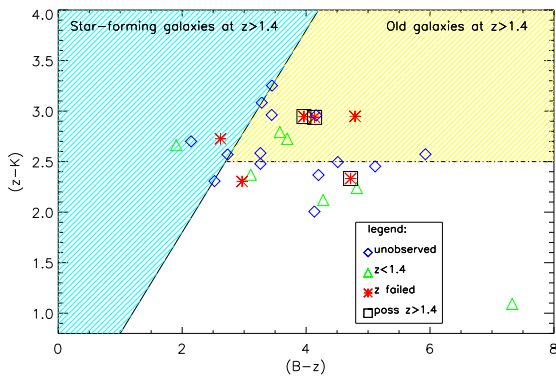


**Figure 5.** Colour-colour  $(z - K)_{AB}$  vs  $(B - z)_{AB}$  diagram for galaxies in the CDF-S. According to Daddi et al. (2004), the region defined by  $(z - K)_{AB} - (B - z)_{AB} \geq -0.2$  (blue shaded area) should isolate  $z > 1.4$  star-forming galaxies. Conversely, the intersection of the regions  $(z - K)_{AB} - (B - z)_{AB} \leq -0.2$  and  $(z - K)_{AB} > 2.5$  should isolate old galaxies with  $z > 1.4$  (yellow shaded area). 4 out of 6 galaxies without redshifts (marked with an asterisk) lie in these regions (although the contamination from lower redshift sources is somewhat higher than the fraction quoted by Daddi et al. (2004)). Sources flagged as potential  $z > 1.4$  sources are overlaid with boxes - 2 out of 3 fulfill the necessary colour criteria.

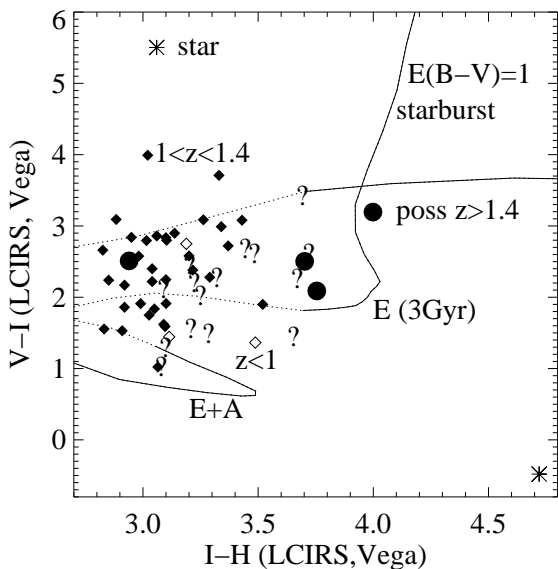


**Figure 6.**  $V - I$  v's  $I - H$  colour-colour diagram. Only galaxies with spectroscopically identified redshifts with class  $> 1$  are shown. Open diamonds are  $z < 1$  galaxies, filled diamonds are  $1 < z < 1.4$ , and large filled circles are unidentified but believed to be at  $z > 1.4$  on the basis of featureless continuum. The remaining unknown redshifts are marked '?'. Galaxy tracks are marked to give an indication of where  $z > 1.4$  galaxies might be expected to lie. The tracks are dotted at  $z < 1.3$  and solid at  $z > 1.3$ .

Four have high confidence quality flags in both samples and agree to within  $\Delta z = 0.001$ . The redshift for the remaining source is unidentified in both surveys. Of the four sources overlapping with the K20 survey (Table 7), three of the redshifts are in agreement, but one which we have flagged as low confidence at  $z=0.99$  is discrepant with the higher  $z=1.553$  K20 estimate.

Matches with the GDDS sample are shown in Table 8. Of the three overlapping sources for which we have confident identifications, one agrees and two disagree. The GDDS confidence rating for one of these failures is  $< 50\%$ . In three cases where our redshift identification is insecure (class 1) and in two cases where we failed, GDDS find higher redshifts ( $z > 1.395$ ) with a high confidence rating, supporting our hypothesis that the redshifts which we failed to get potentially lie at higher- $z$ .

## 5 ANALYSIS

We now turn to addressing the key objectives for the survey set out in §1. Summarizing the situation, using the photometric criteria  $H < 20.5$  and  $I - H > 3.0$ , we have drawn spectroscopic targets from 252 EROs in three LCIR survey fields, of which 159 fall within the field of view of the slit masks employed. We successfully observed a sub-sample of 67 objects drawn randomly from the photometric sample. Spectroscopic identifications were secured for 44 sources (including two stars), a completeness fraction of 66%. We have demonstrated that this large spectroscopic sample is representative of the ERO population in the LCIR survey. The spectra are generally of good quality with higher dispersion than in previous studies (e.g. K20, GDDS).

### 5.1 Redshift Distribution

Our redshift distribution ( $N(z)$ , Figure 3) ranges between 0.755 and 1.4 (with some sources potentially at  $z > 1.4$ ), and therefore demonstrably supports the hypothesis that an  $I - H > 3$  colour criterion is effective in selecting galaxies at  $z \gtrsim 1$  (McCarthy et al. 2001).

Figure 7 compares the observed distribution and that predicted for the larger LCIRS sample using photometric redshifts based on  $UBVR IH$  photometry in the independent LCIRS field HDF-S (Firth et al. 2002). From the latter distribution, Firth et al. concluded that popular semi-analytic models provided a reasonable fit to the overall  $N(z)$  but under-predicted the abundance.

The redshift distribution in our spectroscopic survey varies from field to field with clear structures in each, suggesting significant cosmic variance and clustering among the population. Furthermore, different mixtures of spectral types are seen in the various fields (Table 2). The simplest conclusion consistent with this disparity is that the dominant component of the ERO population is made of luminous spheroidals which are strongly clustered. We will return to analyzing the variance seen across the three fields when we measure the overall spatial clustering in our sample in § 5.5.

Although our spectroscopic redshift distribution is lacking the high- $z$  tail seen in the photometric distribution - due to our incompleteness in the 'spectroscopic desert' - or  $z > 1.4$  regime, we find an overall abundance in agreement

ID	redshift	I mag	FORS2 ID	FORS2 redshift	FORS2 I mag
1276	1.129	22.00	J033219.15-274040.2	1.128	22.25
2681	1.096	21.67	J033237.19-274608.1	1.096	21.98
2800	1.318	23.35	J033239.64-274709.1	1.317	23.69
2158	1.222	22.54	J033230.34-274523.6	1.223	22.89
1792	—	23.48	J033225.76-274347.0	—	24.13

**Table 6.** Redshift comparison with the FORS2 survey in the CDFS field.

ID	redshift	quality flag	K20 id	K20 redshift
2681	1.09600	3	CDFS_00633	1.09600
2158	1.22200	3	CDFS_00507	1.22300
I1843	1.22500	3	CDFS_00547	1.22200
I2163	0.990000	1	CDFS_00139	1.55300

**Table 7.** Redshift comparison with the K20 survey in the CDFS field.

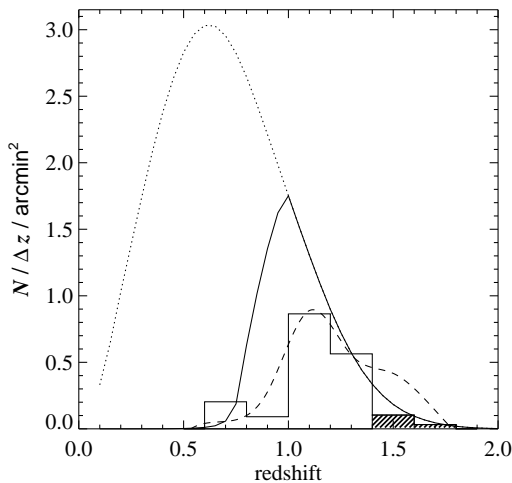


**Figure 7.** Observed redshift distribution for 3 LCIRS fields, corrected for incompleteness (histogram - with shaded region possible  $z > 1.4$  galaxies), compared with that estimated photometrically by Firth et al. (2002; dashed curve) in a fourth field. Overplotted is a predicted  $N(z)$  if EROs produced all ellipticals today via passive luminosity evolution. The local elliptical population has been reverse evolved (assuming all are 5Gyr old), using the luminosity function derived by Nakamura et al (2003) for E/S0 galaxies in the SDSS, which has  $\alpha = -0.83$  (slope),  $\phi^* = 0.0047 * (0.7)^3$  per  $\text{Mpc}^3$ ,  $M^* = -20.75 + 5 * \log_{10}(0.7)$ . The solid curve is the backwards-PLE model including our  $I - H > 3.0$  colour cut, and dotted curve has no colour cut on PLE).

with that found by Firth et al. in the HDF-S, i.e. significantly more than is predicted by semi-analytic models.

## 5.2 $I - H$ versus $R - K$ Colour Selection

Our  $I - H > 3$  selection criterion is different from the frequently-used  $R - K > 5$  (Cimatti et al. 2002) or  $R - K > 6$  (Hu & Ridgway 1994) cut and thus it is interesting to consider whether the greater prominence of early-type spectra (and the larger associated cosmic variance) is due, in part, to

this difference. Our fraction of actively star-forming galaxies ( $\sim 16\%$ ) is much less than that found (50%) in the  $R - K$  selected K20 sample (Cimatti et al. 2002) or the bright K-sample of Yan et al. (2004).

We also might reasonably expect the shorter wavelength baseline of  $I - H$  (compared to  $R - K$ ) to provide an increased sensitivity to strong age-dependent continuum breaks as opposed to the broader wavelength signatures arising from reddening. Unfortunately, given the different nature and classification methods for the various spectroscopic datasets, it is unclear whether the different fractions of early-type galaxies arises entirely from the colour selection. Part of the difference may arise from the increased signal to noise in our data. For example, although a further 40% of our galaxies reveal modest  $[\text{O II}]$  emission, our spectra enable us to clearly demonstrate an underlying old stellar population, whereas such galaxy types may previously have been classified as dust-reddened starbursts. Figure 1 also demonstrates that E+A galaxies, such as appear in our sample (for example, with 5% burst mass in the last 100 Myr) would not be expected in a selection based on  $R - K > 5$  colour cut.

## 5.3 Spectroscopic Properties of the ERO Population

We now turn to the important question of the nature of the ERO population as revealed by the Keck spectra. Thus far we have categorized each spectrum according to its appearance, deferring any astrophysical interpretation of the various classifications. Our goal is to address the relevance of the E, E+A, E+e, E+A+e and late types introduced in §4.1 as well as the homogeneity of the overall ERO population. We stress that our analysis in this section will be illustrative given that the spectroscopic data alone cannot separate uniquely many of the key variables e.g. the effects of age, metallicity and complex star formation histories (c.f. McCarthy et al. 2004).

We begin by stacking the spectra according to our basic classification scheme. Figure 9 shows the result of this coaddition for the higher quality spectra selected with quality flags 2 or 3. In practice, given we used both DEIMOS and LRIS spectrographs, we restricted the coaddition of the

ID	redshift	quality flag	GDSS ID	GDSS redshift	GDSS I mag	GDSS confidence
3253	1.153	2	23.25	SA22-0062	1.154	[O II]
2260	0.798	2	22.99	SA22-0448	1.202	<50%
2467	1.032	3	22.12	SA22-2548	1.022	certain
1655	1.199	1	23.39	SA22-0674	1.493	>75%
1920	1.142	1	23.69	SA22-1983	1.488	95%
3378	0.762	1	23.38	SA22-0107	1.448	single emission line
2335	—	0	23.37	SA22-0398	1.395	95%
2593	—	0	23.01	SA22-0189	1.490	95%
1535	—	0	23.45	SA22-0948	1.396	none/best guess
1792	—	0	23.31	SA22-0721	1.483	none/best guess
1803	—	0	23.37	SA22-0717	2.060	none/best guess

**Table 8.** Redshift comparison with the GDSS survey in the SSA22 field.

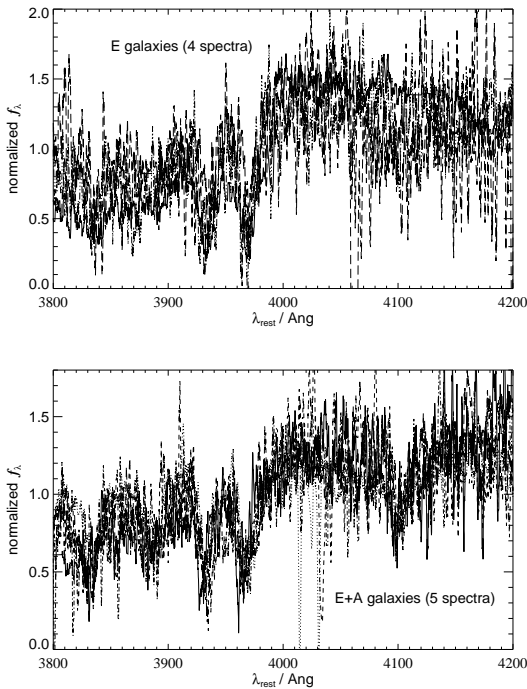


**Figure 8.** Noise spectrum for the E (top) and E+A (bottom) composite spectra, composed of the individual spectra normalised to the same continuum flux and overlaid. The standard deviation in this spectrum is then the error on the composite spectrum.

E, E+A and E+e spectra, for which absorption line measures are particularly helpful, to those taken with the superior resolution DEIMOS, rebinned to a final dispersion of  $3.5\text{\AA}\text{pixel}^{-1}$ . In the case of the late-type spectra, as most examples occur in the LRIS sample, we restricted the coaddition to those taken with LRIS rebinned to  $13.6\text{\AA}\text{pixel}^{-1}$ . We find the error on each composite spectrum to be the deviation in the spectra when each is normalised to the same relative flux in the wavelength range  $3800\text{--}4200\text{\AA}$ . The noise spectra for the E and E+A galaxies are shown in Figure 8, we use this to deduce the error on diagnostics such as the D4000 break and line equivalent widths.

We now briefly discuss the coadded spectra in turn:

### 5.3.1 Pure early type (E)

About 30% of our sample are in the E category and our luminosity-weighted mean spectrum has a  $4000\text{\AA}$  break  $D_{4000} \sim 1.7^6$ . Comparing this with the hypothesis of a simple stellar population following a single burst in the context of Bruzual & Charlot (2003) models we find an average age of  $\sim 2\text{ Gyr}$  at the mean redshift of  $\bar{z}=1.2$ , assuming solar metallicity (Figure 11a). This implies a formation epoch of  $z > 2$  for this subset of the ERO population. This result agrees with McCarthy et al. (2004) who find a  $\langle z_f \rangle = 2.4$  for 20 red galaxies with  $z > 1.3$  in the GDSS, and deduce an early and rapid formation for a substantial fraction of these. Furthermore, Cimatti et al. (2002,2003,2004) deduce formation redshifts between 2–3.4 for similar objects found in the K20 survey.

### 5.3.2 Intermediate age (E+A)

A significant fraction of our sample have strong Balmer absorption lines in addition to prominent  $4000\text{\AA}$  breaks and are indicative of secondary star-formation. These galaxies have traditionally been referred to as E+A galaxies (also known as ‘K+A’; Dressler et al. 1999 ; see also Blake et al. 2004 and refs. therein). Although  $\sim 30\%$  of our absorption line sample fall in this category, the fraction shows considerable field-to-field dispersion (0-50% across the 3 LCIRS fields). Nonetheless, the rate of occurrence is much higher than in nearby field galaxies.

Zabludoff et al. (1996) find 0.6% of all galaxies at  $z \sim 0$  in the Las Campanas Redshift Survey to be E+A (as selected by  $\text{EW}(\text{H}\delta) > 4.5\text{\AA}$ ). Given that EROs make up about  $\sim 10\%$  of the overall galaxy population at our limiting magnitude, we find more than twice as many E+As at  $z \sim 1$ . With a stricter criterion, ( $\text{EW}(\text{H}\delta) > 5\text{\AA}$ ) Goto (2005) finds a local E+A incidence of  $\sim 0.1\%$  in the Sloan Digital Sky Survey (SDSS; York et al. 2000). Bearing in mind that our selection function for EROs is picking out only E+A galaxies which are spheroidal in origin (locally, E+As are found to also have late-type spiral progenitors, see e.g. Blake et al. 2004, Zabludoff et al. 1996), this is reasonably strong evidence for evolution in the number density of such systems from  $z \sim 1 - 2$  to  $z \sim 0$ .

<sup>6</sup> We define the index  $D_{4000} = f(3750 - 3950\text{\AA})/f(4050 - 4250\text{\AA})$  ((Bruzual 1983)

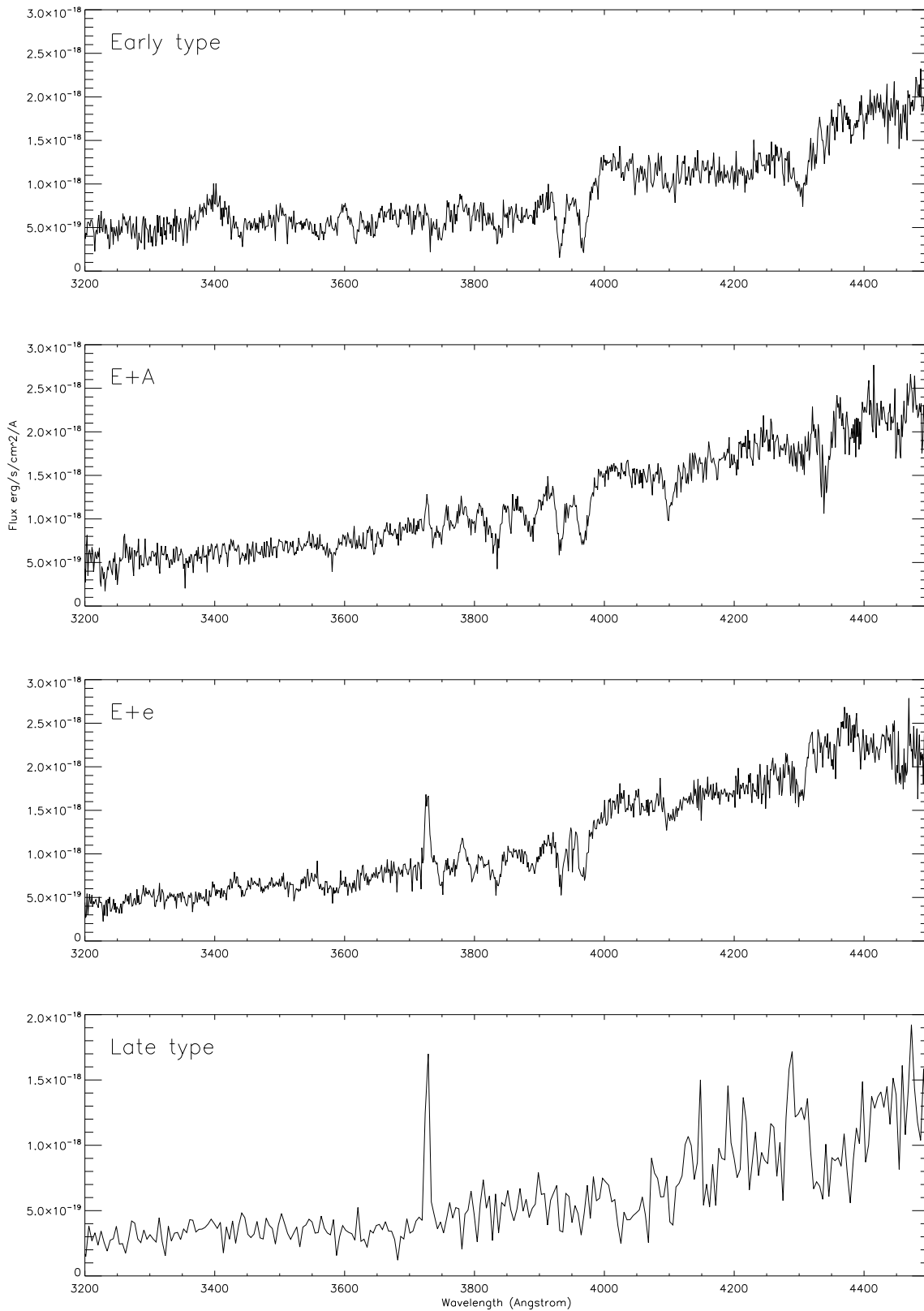
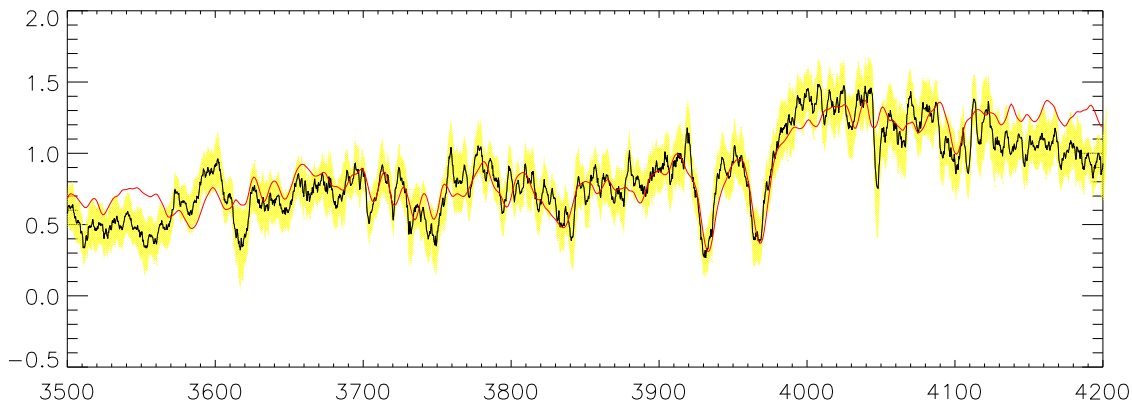
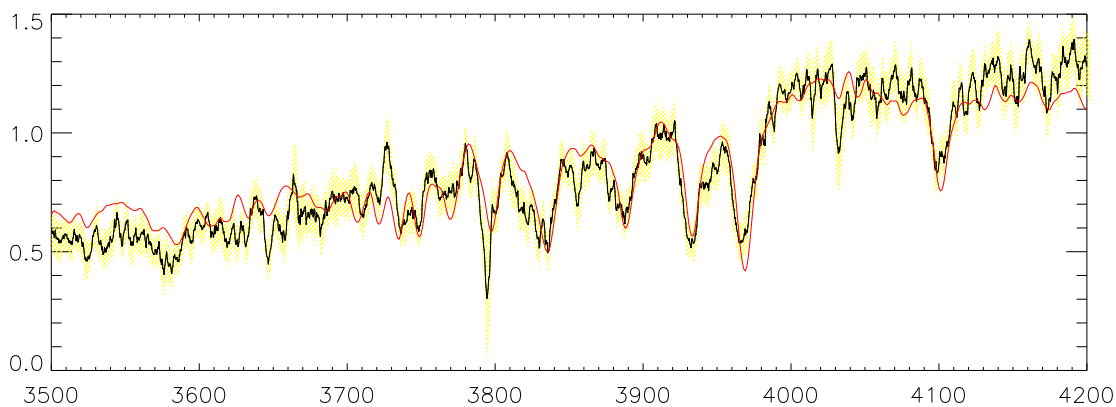


**Figure 9.** Stacked spectra for categories E, E+A, E+e and late type as defined in §4.1. The E, E+A and E+e spectra were drawn from the superior resolution DEIMOS data whereas the late-type spectra were restricted to the LRIS sample. Only spectra with quality flags 2 or 3 were included.



(a)



(b)

**Figure 10.** (a) Pure early type composite spectrum compared to a Bruzual and Charlot (2003) model spectrum (dashed line) of a 3.5Gyr population and (b) the E+A spectrum is well fit by an underlying 2Gyr population, with a 100Myr old secondary burst of 2% by mass. Both assume a Salpeter IMF and solar metallicity. The shaded regions show the errors on the composite spectra, which are the standard deviation of the flux at each wavelength in the individual spectra (scaled to the same relative luminosity).

The composite spectrum (Figure 9) has an average equivalent width  $W_{H\delta} = 6\text{\AA}$ . Figure 11b shows the evolution with age of the  $H\delta$  equivalent width for sub-solar, solar and super-solar metallicities. Combining with the  $D_{4000}$  index (§ 5.3.1, Figure 11) we find the spectrum can be readily interpreted in terms of an underlying population as old as that of the mean E type spectrum discussed above, with an additional secondary component (5-10%) which formed between 30 Myr and 1 Gyr prior to the epoch of observation. This is consistent with examples of star formation activity found in  $z \sim 1$  spheroidals by Treu (2004 and references therein).

In summary, the simplest hypothesis is that the E+A galaxies have a similar origin to the E-type galaxies reflecting that component of the population which recently underwent a secondary burst, possibly associated with a merger. It is possible that the K-bright star forming objects at  $z \sim 2$  seen in GOODS and K20 could be the same objects we are seeing as E+As at  $z \sim 1$ , in their post-burst phase.

### 5.3.3 Active early type (E+e)

As earlier studies in clusters have shown (e.g. Couch & Sharples 1987, Barger et al 1996), for established stellar systems undergoing secondary activity, a subset are likely to show the mixed signals of an old stellar population and emission lines during the active phase. In the case of merger driven evolution, unless the accretion is purely stellar such systems will show diluted evidence of an old stellar population and [O II] emission. Depending on the duty-cycle, the Balmer absorption lines will be partially or wholly filled by gaseous emission. In fact, although Balmer absorption lines are undetected amongst each individual spectrum in this class, they are weakly visible in the composite spectrum (Figure 9).

Given our explanation for the E+A sources, it is natural to adopt the above explanation for many of the E+e spectra whose line properties are understandably more diverse.

In summary, the dominant component of our ERO sam-

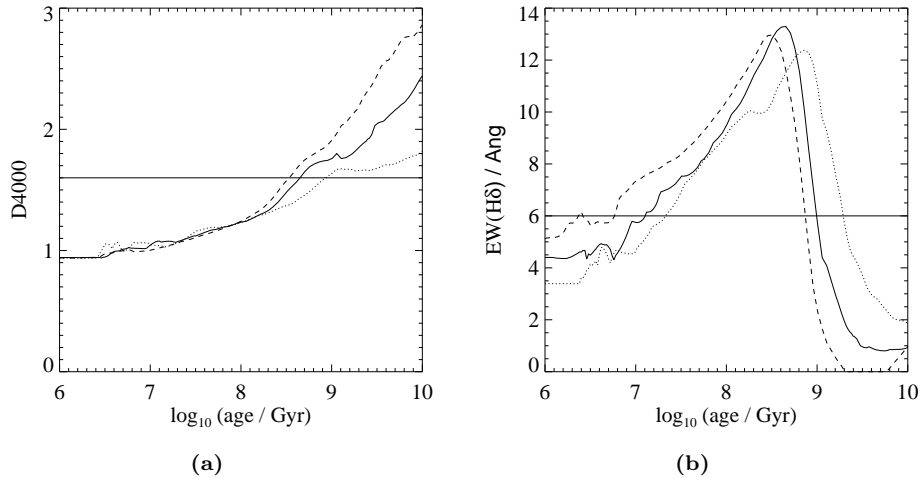


**Figure 11.** (a) Evolution of  $D_{4000}$  according to a single-burst Bruzual & Charlot (2003) model of solar metallicity (solid line),  $0.2\times$  solar (dotted line) and  $2.5\times$  solar (dashed line). Comparison with the mean early-type spectrum implies an age of  $\sim 1.6$  Gyr at the mean sample redshift  $z \simeq 1.2$ . (b) Evolution of  $EW(H\delta)$  for a single-burst Bruzual & Charlot (2003) model of solar metallicity (solid line),  $0.2\times$  solar (dotted line) and  $2.5\times$  solar (dashed line).

ple consists of old galaxies seen in various stages of intermittent, but minor, activity. Figure 12 shows an exemplary star formation cycle which may give rise to the various stages of evolution we observe in our sample. The E type spectra of old galaxies are formed at high redshift, perhaps in an initial discrete burst of star formation. Some time later a secondary burst is triggered, giving rise to the [OII] emission seen in the E+e spectra, and subsequently Balmer absorption lines become visible once star formation has been truncated, in the E+A class. The mixed populations seen, which are predominantly E+A with [OII] emission, represent some intermediate stage between E+e and E+A. Barger et al. (1996) successfully explain the numbers of systems similar to those discussed above in clusters at low redshift ( $z=0.31$ ) using models involving secondary bursts of star formation over the 2 Gyr prior to the epoch of observation. Treu et al. (2005) have recently demonstrated that the star formation history of field spheroidals is heavily dependent on their mass. If galaxy formation is governed by a ‘down-sizing’ mechanism (Cowie et al. 1996), i.e. growth through rapid star-formation trends smoothly to less massive galaxies with decreasing redshift, then in a large sample we might expect the E, E+A, E+A+e and E+e galaxies to be progressively ordered in decreasing luminosity (e.g. in the rest-frame  $I-H$  band). We examined our data, unsuccessfully, for evidence of such a trend. It may be that all of these galaxies formed the bulk of their mass at high- $z$  and that subsequently environment plays a bigger role, with mergers or interactions triggering more recent complex star formation histories.

#### 5.3.4 Late Type

A small fraction ( $\sim 16\%$ ) of our sample are classed as late type on the basis of prominent [O II] emission together with weak or non-existent Ca II H&K absorption. In these systems, the luminosity weighted stellar population is clearly young and star-forming.

In the co-added LRIS spectrum of 4 late-type galaxies in

SSA22, we find an average line flux of  $1 \times 10^{-17} \text{ ergs}^{-1} \text{ cm}^{-2}$ . At the average redshift  $z=1.2$ , this equates to a fairly modest star formation rate (SFR) of  $1.1 \pm 0.3 \text{ M}_{\odot} \text{ yr}^{-1}$  using Kennicutt’s (1998) conversion:

$$SFR(\text{M}_{\odot} \text{ yr}^{-1}) = (1.4 \pm 0.4) \times 10^{-41} L([\text{OII}]) (\text{ergs}^{-1})$$

However this may be a lower limit as it is uncorrected for extinction which presumably is responsible for the red  $I-H$  colour. As an illustration, a ‘pure’ dusty starburst (with no significant flux contribution from an underlying older population) our  $I-H > 3$  selection criterion requires  $E(B-V) \gtrsim 1$  (Figure 1). In the simplest case where dust screens the gas and stars by equal amounts, this would imply a correction to the SFR as large as  $\gtrsim 50$  ( $\sim 100 \text{ M}_{\odot} \text{ yr}^{-1}$ ). In practice, of course, there are numerous uncertainties in deriving star formation rates in this manner. The recent Spitzer results of Yan et al. (2004) imply high extinction for the late type red galaxies and typical star formation rates  $50 - 170 \text{ M}_{\odot} \text{ yr}^{-1}$ .

#### 5.4 Abundance of Galaxies with Established Stellar Populations

The foregoing discussion has revealed that the bulk of our  $I-H > 3$  sample, specifically most of those in the dominant spectral categories E, E+A and E+e, contain well-established stellar populations (defined broadly as those where the bulk of the star formation occurred prior to  $z=2$ ). It is thus interesting to make a rough comparison of the luminosity density in this population with that in the population of present day spheroidals.

With a surface area of  $200 \text{ arcmin}^{-2}$  across our 3 LCIRS fields, and assuming a uniform redshift-dependent selection function across the interval  $1.0 < z < 1.35$  (in which 90% of our objects lie) we effectively survey a co-moving volume of  $\sim 1.70 \times 10^4 \text{ Mpc}^3$ . The average space density of EROs is thus  $\phi \approx 1 \times 10^{-3} \text{ Mpc}^{-3}$  of which we estimate  $\sim 75\%$  contain an established stellar population. At the median redshift  $z=1.2$ , our  $H < 20.5$  magnitude limit corresponds to an absolute

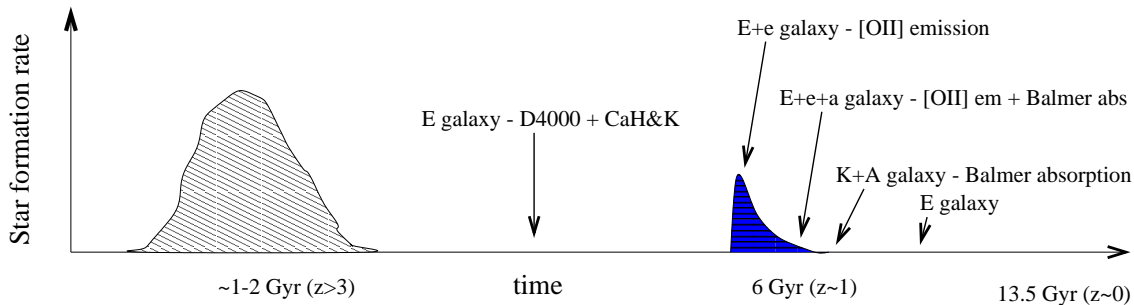


**Figure 12.** Diagram showing a cycle of star formation activity which would explain the observed spectra of the E, E+e, E+A and E+A with [OII]. The E type galaxies are formed in an initial discrete burst of star formation, some time later a secondary burst gives rise to the [OII] emission seen in the E+e spectra and subsequently Balmer absorption lines once star formation is truncated.

rest-frame I-band luminosity of  $M_I = -21.85$ , equivalent in local terms (Blanton et al. 2003) to  $\simeq 1.25L^*$ .

According to the Bruzual & Charlot (2003) models discussed in §5.3, an established stellar population will passively fade by  $\simeq 1$  magnitude in rest-frame  $I$  since  $z \simeq 1.2$  (e.g. Fontana et al. 2004). Accordingly, in the absence of growth by accretion (Treu et al 2004), our survey sensitivity corresponds to locating the progenitors of current epoch  $0.6L^*$  galaxies. Our inferred abundance of  $\phi(L > 0.6L^*) = 0.6\phi^* = 3 \times 10^{-3} \text{Mpc}^{-3}$ , or just over a half of all galaxies today.

We thus find agreement with Firth et al. (2002) that the ERO population is sufficient to explain  $\sim 50\%$  the present-day spheroidal population solely via passive evolution. This is consistent with purely photometric determinations of the evolving red rest-frame luminosity function (e.g. Chen et al. 2004) and both spectroscopic and photometric measures of the evolving mass density in red systems (e.g. Glazebrook et al. 2004; Bell et al. 2004; Fontana et al. 2004). While the most up-to-date semi-analytic hierarchical merging models (e.g. Somerville et al. 2004) can produce the required number density of massive systems at  $z \sim 2$ , they have great difficulty in reproducing the high space density of massive galaxies with red colours and evolved stellar populations.

### 5.5 Clustering of the ERO Population

One of the motivations for defining the redshift distribution of the ERO population is to better understand their spatial clustering. McCarthy et al (2001) measured the angular clustering of the  $I - H > 3$  population in the HDF-S and CDF-S field, a total area of  $0.39 \text{ deg}^2$ . Within the range appropriate for verification via our study ( $19 < H < 20.5$ ), they found an amplitude  $\theta_0 = 6.7 \pm 0.4 \text{ arcsec}$  for the two-point correlation function (assuming a form  $w(\theta) = (\theta_0/\theta)^{\gamma-1}$  where the slope of the correlation function  $\gamma$  is  $-1.8$  as in local samples). To invert the angular function and its normalization  $\theta_0$  into its spatial equivalent for comparison with local sources, McCarthy et al adopted a Gaussian  $N(z)$  with a peak at  $z=1.2$  and a dispersion  $\sigma_z=0.3$ . They obtained a clustering length  $r_0=9.8 h^{-1} \text{ Mpc}$  - a value considered to be larger than that for present day galaxies but comparable to that for the local elliptical population (Norberg et al 2001).

Firth et al (2002) subsequently analyzed the angular clustering more rigorously in the HDS-S field. For a  $H < 20.5$  sample of 170 galaxies with  $I - H > 3$  across a smaller area

of  $0.21 \text{ deg}^2$  a more refined photometric redshift distribution was derived. They relate the correlation length  $r_0$  at a given redshift  $z$  to its zero redshift equivalent, say  $r_{z0}$ , via the expression:

$$r_0(z) = r_{z0} (1 + z)^{(\gamma - \epsilon - 3)/\gamma}$$

where  $\epsilon$  parameterizes the evolution of clustering.  $\epsilon=0$  corresponds to constant clustering in proper space and  $\epsilon = -1.2$  constant clustering in comoving coordinates. Assuming their ERO population did not evolve in comoving terms (i.e.  $\epsilon=-1.2$ ), Firth et al deduced the population would have a local clustering with  $r_{z0}=7.5 \pm 3.7$ , i.e. 1.5 times larger than local galaxies but similar to that observed ( $r_{z0} \simeq 6-8 \text{ Mpc}$ ) for local ellipticals. Most significant of all, the clustering of the ERO sample in both studies is a factor of 2.5-4 times stronger than the full  $H$ -selected population. The larger error bar on the Firth et al determination compared to McCarthy et al is only partly due to the smaller field employed; it also reflects a more realistic measure of the overall inversion uncertainty.

The availability of spectroscopic redshifts allows us to strengthen these conclusions in two ways. Firstly, the improved precision of a spectroscopic redshift over its photometric equivalent permits us to directly detect large scale structures composed of EROs rather than relying entirely on projected angular statistics. Secondly, the deduced redshift distribution,  $N(z)$  (see §4) allows us to significantly improve upon the clustering analyses undertaken by McCarthy et al and Firth et al.

To illustrate the former, our spectroscopy, when combined with those selected with  $R - K > 5$  in the FORS2 sample (Vanzella et al (2004)) define a prominent overdensity of EROs at  $z=1.22$  in the CDFS (Figure 13). The angular distribution of 20 sources within  $\delta z = \pm 0.01$  (i.e. a velocity dispersion of  $\sim 400 \text{ km s}^{-1}$ ) is shown in Figure 14 and appears to trace a large wall-like structure possibly consistent with an assembling cluster. The five LCIRS galaxies in the structure all exhibit signs of a prominent old stellar population, whereas the majority in the FORS2 sample were spectroscopically identified by [O II] emission alone. This discrepancy *may* be explained by our selection function for EROs. However, assuming that this is a gravitationally bound cluster, we speculate that the relative spatial concentrations of the two galaxy types might also be evidence for the morphology-density relation (Dressler et al. 1997) oper-

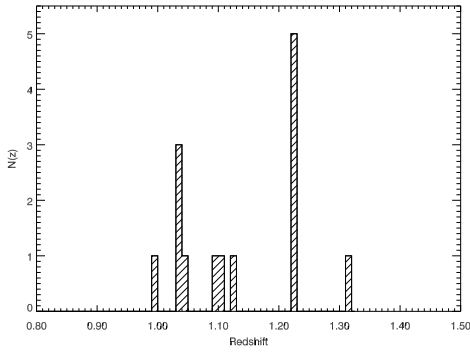


**Figure 13.** Large Scale Structure in the CDFS (including sources selected using  $R-K > 5$ ). The bin size is  $\Delta z = 0.02$  ( $400\text{km s}^{-1}$ ).

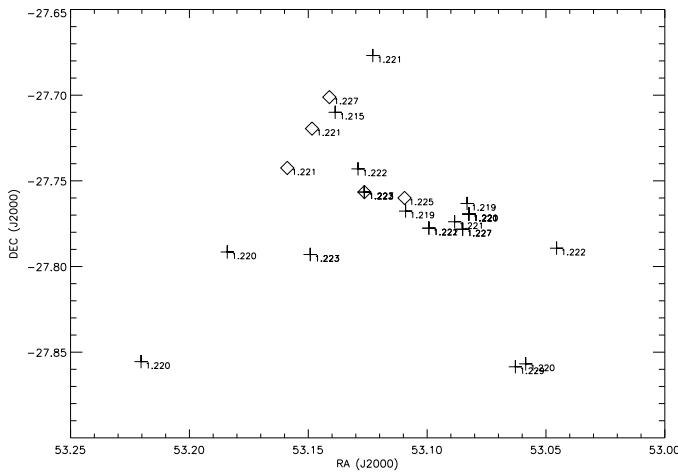


**Figure 14.** Angular distribution of galaxies around the  $z = 1.22 \pm 0.01$  structure in the CDFS. Each galaxy is labelled with its spectroscopic redshift. Crosses represent sources in the FORS2 sample, diamonds those from the present survey.

ating at higher redshift. In summary, we are possibly seeing the older, evolved galaxies at the centre of the cluster and the more active star-forming galaxies tracing the outskirts. Assuming further that the cluster is virialized, we find a mass of  $\sim 5.6 \times 10^{14} M_{\odot}$  within a radius of 5 Mpc. This is consistent with other high redshift clusters, for example, the rich cluster MS1054-03 which has a mass of  $\sim 1.9 \times 10^{15} M_{\odot}$  within  $\sim 2$  Mpc (Tran et al. 1999).

Returning finally to the spatial correlation function, we can verify more precisely the discussion in Firth et al (2002) by comparing the photometrically-inferred redshift distribution  $N(z)$  for a  $H < 20.5$ ,  $I - H > 3.0$  sample (Figure 29 in Firth et al’s paper) with our spectroscopic equivalent (Figure 6). As we have already noted, the distributions are remarkably similar so we can expect little change in the analysis of Firth et al.

However, taking the angular clustering signal from the larger area studied by McCarthy et al (2001), we infer an amplitude for the angular correlation function  $w(\theta)$  at  $\theta=1.0$  arcmin of  $A=0.173 \pm 0.010$  (c.f.  $0.20 \pm 0.06$  from Firth et

al’s HDF-S study) and using the redshift distribution of Figure 6, this inverts to a local clustering scale length for the comoving case of  $r_{z0} = 6.5 \pm 0.4$ . This is somewhat smaller than the amplitude claimed by Firth et al but a more precise estimate.

Our measurement is slightly smaller, but potentially more accurate, than most  $r_0$  amplitudes in the literature relying on photometric redshift estimates. For example, Daddi et al. (2002) quote a range  $5.5 \lesssim r_0/(h^{-1} \text{Mpc}) \lesssim 16$  (note they use  $H_0 = 100h$ ) for old passively evolving EROs. Brown et al. (2005) estimate the spatial clustering of EROs over a large area ( $0.98^2$  degrees) in the NOAO Deep Wide Field Survey, using photometric redshifts, and extrapolate a value of  $r_0 \sim 7.5h^{-1} \text{Mpc}$  for  $K \gtrsim 20$ , where  $H_0 = 100h$ .

## 6 CONCLUSIONS

We have used  $H$ -band imaging from the LCIRS survey to select a large and uniform sample of EROs brighter than  $H > 20.5$  with a colour selection  $(I - H) > 3$ , over three fields (SSA22, CDFS & NTT Deep Field).

Our deep Keck LRIS & DEIMOS spectroscopy has targetted 50% of these EROs over a sampling area of  $200 \text{arcmin}^2$ . Of the 67 EROs appearing on our slitmasks, we have determined reliable spectroscopic redshifts for 44 – a completeness fraction of 66%. This is the most extensive spectroscopic study of this population to date, and the first to focus on an  $H$ -band selection. Most of our spectra have a continuum signal/noise of 2–3 per  $\text{\AA}$  and the superior resolution of our DEIMOS data enables us to undertake diagnostic spectroscopic studies of various subsets of the ERO population.

We find that most of the ERO population contain a clear signature of an old stellar population. In contrast to other studies, based on smaller samples with weaker signal/noise and lower dispersion data, only a minority of our sample (16%) appears to be due to genuinely young dust-reddened systems. We suggest the discrepancy may arise in part because of our choice of  $I - H$  as a colour discriminant rather than the coarser  $R - K$ .

However, within our dominant population of established galaxies, we notice a great diversity in spectral properties. We classify these as pure E (27%), E+A (13.5%), E+e (23%) and ‘mixed’ E+A+e (13.5%) depending on the presence or otherwise of secondary features of star formation such as [O II] emission and post-burst Balmer absorption. We propose that these different subsets represent various manifestations of the same overall population seen at different stages as they accrete associated objects and via illustrative spectral modelling deduce that the bulk of the stars in the population formed well before  $z \simeq 2$ .

The abundance of the E+A and similar systems in our sample is an extremely interesting result. The numbers are quite high, in comparison with the local universe where they are very rare, and imply we may be seeing the fading light of a recent major star formation epoch.

As earlier papers in this series have surmised, the abundance and luminosity distribution of this established component of EROs, when faded by passive evolution to the present epoch, cannot account for the population of local early-type galaxies. As many workers are deducing (Treu et

al 2005, Bundy et al 2005), continued growth and transformations are required over  $0.5 < z < 1.5$  to match the local distribution. However, as many authors have claimed, the evolutionary growth in the number of early-types since  $z < 4$  is far less dramatic than that predicted in recent semi-analytical models.

We finally refine earlier estimates of the spatial clustering of this population taking into account the improved redshift distribution in the inversion from the angular clustering seen in the overall LCIRS survey. We find a spatial correlation length, corrected to the present epoch assuming no evolution in comoving coordinates, of  $r_0 = 6.5 \pm 0.4 h^{-1}$  Mpc, a signal comparable to but marginally less than that seen in present day ellipticals.

## ACKNOWLEDGMENTS

We acknowledge the LCIRS collaboration for the provision of an unique database upon which this detailed spectroscopic study was based. In particular, we are indebted to Hsiao-Wen Chen, Andrew Firth, Richard McMahon, Chris Sabbey and Ofer Lahav for their important contributions. The CIRS camera was made possible by the generous support of the Raymond and Beverly Sackler Foundation.

We also thank various individuals in the Keck community for their assistance. We thank Sandy Faber, Judy Cohen, Chuck Steidel and the DEIMOS/LRIS teams for making these impressive instruments a reality. The software used to design the slitmasks was written by Drew Phillips. The LRIS slitmask data reduction IRAF package, BOGUS, was written by Daniel Stern, S. Adam Stanford & Andrew Bunker. The DEIMOS data analysis pipeline was developed at UC Berkeley with support from NSF grant AST-0071048. We are grateful to Michael Cooper & Alison Coil for their advice in the use of this package.

Data presented herein were obtained at the W. M. Keck Observatory, which is operated as a scientific partnership among the California Institute of Technology, the University of California, and the National Aeronautics and Space Administration. The Observatory was made possible by the generous financial support of the W. M. Keck Foundation.

We thank Stephane Charlot & Gustavo Bruzual for making their useful stellar population synthesis code available. MD is grateful for support from the Fellowship Fund Branch of AFUW Qld Inc., the Isaac Newton Studentship, the Cambridge Commonwealth Trust and the University of Sydney.

Finally, we thank the referee, Andrea Cimatti, for detailed constructive comments which have improved the paper, and Karl Glazebrook, for some helpful comments on the manuscript.

## REFERENCES

- Abraham R. G., Glazebrook K., McCarthy P. J., Crampton D., Murowinski R., Jørgensen I., Roth K., Hook I. M., Savaglio S., Chen H., Marzke R. O., Carlberg R. G., 2004, *AJ*, 127, 2455
- Arnouts S., D’Odorico S., Cristiani S., Zaggia S., Fontana A., Giallongo E., 1999, *A&A*, 341, 641
- Barger A. J., Aragon-Salamanca A., Ellis R. S., Couch W. J., Smail I., Sharples R. M., 1996, *MNRAS*, 279, 1
- Beckett M. G., Mackay C. D., McMahon R. G., Parry I. R., Ellis R. S., Chan S. J., Hoenic M., 1998, in *Proc. SPIE Vol. 3354*, p. 431-435, *Infrared Astronomical Instrumentation*, Albert M. Fowler; Ed. CIRS: progress with the Cambridge infrared survey instrument. pp 431-435
- Blake C., et al. 2004, *MNRAS*, 355, 713
- Blanton M. R., et al., 2003, *ApJ*, 592, 819
- Brown, M. J. I., Jannuzi, B. T., Dey, A., & Tiede, G. P. 2005, *ApJ*, 621, 41
- Bruzual G., Charlot S., 2003, *MNRAS*, 344, 1000
- Bruzual A. G., 1983, *ApJ*, 273, 105
- Bundy K., Fukugita M., Ellis R. S., Kodama T., Conselice C. J., 2004, *ApJ*, 601, L123
- Bunker A. J., Stanway E. R., Ellis R. S., McMahon R. G., McCarthy P. J., 2003, *MNRAS*, 342, L47
- Chen H., et al., 2002, *ApJ*, 570, 54
- Cimatti A., Andreani P., Rottgering H., Tilanus R., 1998, *Nature*, 392, 895
- Cimatti A., et al., 2002, *A&A*, 381, L68
- Cimatti A., et al., 2004, *Nature*, 430, 184
- Couch W. J., Sharples R. M., 1987, *MNRAS*, 229, 423
- Cowie L. L., Gardner J. P., Lilly S. J., McLean I., 1990, *ApJ*, 360, L1
- Cowie L. L., Songaila A., Hu E. M., Cohen J. G., 1996, *AJ*, 112, 839
- Daddi E., et al., 2002, *A&A*, 384, L1
- Daddi E., Cimatti A., Renzini A., Fontana A., Mignoli M., Pozzetti L., Tozzi P., Zamorani G., 2004, *ApJ*, 617, 746
- Dey A., Graham J. R., Ivison R. J., Smail I., Wright G. S., Liu M. C., 1999, *ApJ*, 519, 610
- Dickinson M., Giavalisco M., The Goods Team 2003, in *The Mass of Galaxies at Low and High Redshift The Great Observatories Origins Deep Survey*. pp 324+
- Dressler A., Oemler A. J., Couch W. J., Smail I., Ellis R. S., Barger A., Butcher H., Poggianti B. M., Sharples R. M., 1997, *ApJ*, 490, 577
- Dressler A., Smail I., Poggianti B. M., Butcher H., Couch W. J., Ellis R. S., Oemler A. J., 1999, *ApJS*, 122, 51
- Dunlop J., Peacock J., Spinrad H., Dey A., Jimenez R., Stern D., Windhorst R., 1996, *Nature*, 381, 581
- Eisenstein D. J., et al., 2003, *ApJ*, 585, 694
- Elston R., Rieke G. H., Rieke M. J., 1988, *ApJ*, 331, L77
- Elston R., Rieke M. J., Rieke G. H., 1989, *ApJ*, 341, 80
- Faber S. M., et al., 2003, in *Instrument Design and Performance for Optical/Infrared Ground-based Telescopes*. Edited by Iye, Masanori; Moorwood, Alan F. M. *Proceedings of the SPIE*, Volume 4841, pp. 1657-1669 (2003). The DEIMOS spectrograph for the Keck II Telescope: integration and testing. pp 1657-1669
- Firth A. E., et al., 2002, *MNRAS*, 332, 617
- Fontana A., et al., 2004, *A&A*, 424, 23
- Giacconi R., et al., 2002, *ApJS*, 139, 369
- Giavalisco M., et al., 2004, *ApJ*, 600, L93
- Glazebrook K., et al., 2004, *Nature*, 430, 181
- Goto T., 2005, *MNRAS*, pp 53+
- Graham J. R., Dey A., 1996, *ApJ*, 471, 720
- Hu E. M., Ridgway S. E., 1994, *AJ*, 107, 1303
- Lilly S. J., Le Fevre O., Crampton D., Hammer F., Tresse L., 1995, *ApJ*, 455, 50
- Massey P., Gronwall C., 1990, *ApJ*, 358, 344
- Massey P., Strobel K., Barnes J. V., Anderson E., 1988, *ApJ*, 328, 315
- McCarthy P. J., 2004, *ARA&A*, 42, 477
- McCarthy P. J., et al., 2001, *ApJ*, 560, L131
- McCarthy P. J., et al., 2004, *ApJ*, 614, L9
- McCarthy P. J., Persson S. E., West S. C., 1992, *ApJ*, 386, 52
- Nakamura O., Fukugita M., Yasuda N., Loveday J., Brinkmann

- J., Schneider D. P., Shimasaku K., SubbaRao M., 2003, *AJ*, 125, 1682
- Oke J. B., et al., 1995, *PASP*, 107, 375
- Phillips A. C., Faber S., Kibrick R., Wallace V., DEIMOS Team 2002, *Bulletin of the American Astronomical Society*, 34, 1320
- Somerville R. S., et al., 2004, *ApJ*, 600, L135
- Spinrad H., Dey A., Stern D., Dunlop J., Peacock J., Jimenez R., Windhorst R., 1997, *ApJ*, 484, 581
- Stanway E. R., Bunker A. J., McMahon R. G., Ellis R. S., Treu T., McCarthy P. J., 2004, *ApJ*, 607, 704
- Tran K. H., Kelson D. D., van Dokkum P., Franx M., Illingworth G. D., Magee D., 1999, *ApJ*, 522, 39
- Treu T., 2004, in *Clusters of Galaxies: Probes of Cosmological Structure and Galaxy Evolution The Formation of Early-type Galaxies: Observations to  $z \cong 1$* . pp 178–+
- Treu T., et al., in press, (astro-ph/0502028)
- van Dokkum P. G., Ellis R. S., 2003, *ApJ*, 592, L53
- Vanzella E., et al. 2004, in press, (astro-ph/0406591)
- Yan L., et al., 2004, *ApJS*, 154, 75
- Yan L., Thompson D., Soifer B. T., 2004, *AJ*, 127, 1274
- Yan L., Thompson D. J., Soifer B. T., 2003, *American Astronomical Society Meeting Abstracts*, 203,
- York D. G., et al., 2000, *AJ*, 120, 1579
- Zabludoff A. I., Zaritsky D., Lin H., Tucker D., Hashimoto Y., Shectman S. A., Oemler A., Kirshner R. P., 1996, *ApJ*, 466, 104

